

Origin of (2014) MU₆₉-like Kuiper-belt contact binaries from wide binaries

Evgeni Grishin¹, Uri Malamud¹, Hagai B. Perets¹, Oliver Wandel², Christoph M. Schäfer²

¹*Physics Department, Technion - Israel Institute of Technology, Haifa, Israel 3200002*

²*Institut für Astronomie und Astrophysik, Eberhard Karls Universität Tübingen, Auf der Morgenstelle 10, 72076 Tübingen, Germany*

Following its flyby and first imaging the Pluto-Charon binary, the New Horizons spacecraft visited the Kuiper-Belt-Object (KBO) (486958) 2014 MU₆₉ (Arrokoth). Imaging showed MU₆₉ to be a contact-binary, made of two individual lobes connected by a narrow neck, rotating at low spin period (15.92 h), and having high obliquity ($\sim 98^\circ$)¹, similar to other KBO contact-binaries inferred through photometric observations². The origin of such peculiar configurations is puzzling, and all scenarios suggested for the origins of contact-binaries³⁻⁵ fail to reproduce such properties and their likely high frequency. Here we show that semi-secular perturbations^{6,7} operating only on ultra-wide ($\sim 0.1 - 0.4$ Hill-radius⁸) KBO-binaries can robustly lead to gentle, slow-speed binary mergers at arbitrarily high obliquities, but low rotational velocities, that can reproduce MU₆₉'s (and similar oblique contact binaries) characteristics. Using N-body simulations, we find that $\sim 15\%$ of all ultra-wide binaries with cosine-uniform inclination distribution^{5,9} are likely to merge through this process. Moreover, we find that such mergers are sufficiently gentle as to only slightly deform the KBO shape, and can produce the measured rotation speed of MU₆₉. The semi-secular contact-binary for-

mation channel not only explains the observed properties of MU₆₉, but could also apply for other Kuiper/asteroid belt binaries, and for Solar/extra-solar moon systems.

The discovery of MU₆₉'s bilobate shape and peculiar configuration opens new avenues of exploration and provide new clues on the physical processes that sculpture the Solar-System. Here we describe a novel evolutionary channel for the formation of MU₆₉ from an initially wide binary, producing MU₆₉-like objects. We consider the initial binary to be a member of a hierarchical triple together with the Sun. Due to secular evolution induced by the Sun, the inner orbit may experience changes in its eccentricity and mutual inclination on secular time-scales much longer than their orbital periods, known as Lidov-Kozai (LK) oscillations, which can be modelled using a secular orbit averaging approach^{10,11}. Large LK-oscillations take place when the mutual inclination is large ($40^\circ \lesssim i \lesssim 140^\circ$). The highest eccentricities are attained as the binary evolves to the lowest inclinations and vice-versa¹².

If the binary eccentricity exceeds a threshold e_{coll} , the small pericentre allows binary collisions. Thus, LK evolution could lead to coalescence of individual Kuiper-Belt-Binary (KBB) members into a single, likely irregularly shaped KBO⁵. However, since the closest approach occurs concurrently with the lowest inclinations, collisions mostly occur near $i \approx 40^\circ, 140^\circ$ ¹³. Moreover, tidal effects and the non-spherical structure of the KBB components quench LK evolution, which makes collision possible only at a small part of the parameter space^{5,14}. The standard LK mechanism is therefore disfavoured for the origin of the highly-oblique MU₆₉, but can explain the origin of highly eccentric KBBs such as WW31 and 2001 QW322^{5,15,16}.

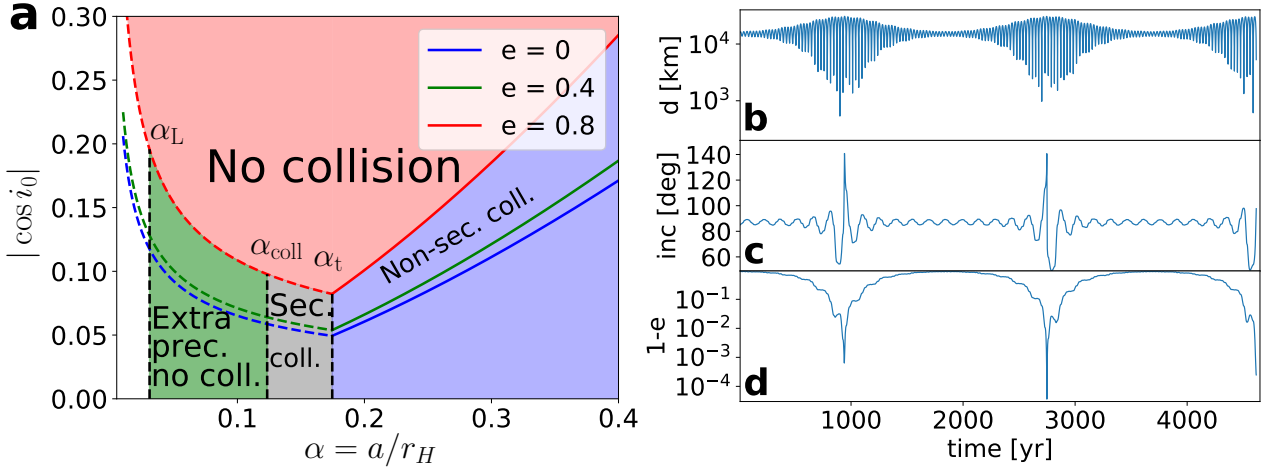


Figure 1: | **Roadmap to collisions of MU₆₉.** (a), The orbital evolution of MU₆₉ in initial separation/initial inclination space. The initial eccentricity is (from bottom to top lines) 0 (blue), 0.4 (green) and 0.8 (red). Solid lines show the condition for a non-secular collisions (Eq. 14) with an unbound eccentricity. Dashed lines show the conditions for a secular collision (Eq. 4) and a deterministic eccentricity. The different domains are as follows: White - LK oscillations are completely quenched and the eccentricity is constant, $\alpha < \alpha_L$ (Eq. 9). Green - the eccentricity is excited, but below e_{coll} , and collisions are avoided, $\alpha_L < \alpha < \alpha_{\text{coll}}$ (Eq. 12). Grey - secular evolution can lead to a collision, $\alpha_{\text{coll}} < \alpha < \alpha_t$ (Eq. 1). Blue - non-secular perturbations dominate and lead to a collision. Red - the initial inclination is too low to induce a collision. (b)-(d), Time evolution of the instantaneous distance, inclination and eccentricity of an individual orbit with initial Keplerian elements of semi-major axis $a = 0.3r_H$, eccentricity $e = 0.1$, inclination $i = 86^\circ$, argument of periape $\omega = 0$, argument of ascending node $\Omega = \pi/4$ and mean anomaly $\mathcal{M} = 0$. The outer binary is set at $\omega_{\text{out}} = \Omega_{\text{out}} = 0$ and $\mathcal{M}_{\text{out}} = -\pi/4$.

When the inner-to-outer period ratio increases, secular averaging breaks down, and the evolution is no longer secular, but only semi-secular. The inner-binary now evolves significantly during the outer-orbit timescale, and short-term fluctuations arise, making the LK evolution more complex^{6,7,17}. The maximal eccentricity can be calculated analytically, including domains where it is unconstrained⁷ and the evolution is non-secular. Fig. 1a shows the analytical 2D parameter space for allowed and forbidden domains for collisions in terms of the initial inclination $\cos i_0$ and the initial separation of the inner binary normalized to the Hill radius $r_H = a_{\text{out}} (m_{\text{in}}/3M_{\odot})^{1/3}$, where $\alpha \equiv a/r_H \lesssim \alpha_H = 0.4$ is the Hill-stability limit for highly inclined orbits⁸. We use the outer orbit parameters of MU₆₉: semi-major axis $a_{\text{out}} = 44.581$ au and eccentricity $e_{\text{out}} = 0.041$. We model the lobes as triaxial ellipsoids of dimensions approximately $22 \times 20 \times 7$ and $14 \times 14 \times 10$ km³¹, leading to a total radius of $R_{\text{tot}} = 18$ km and inner mass of $m_{\text{in}} = (1.61+1.03) \cdot 10^{18}$ g = $2.64 \cdot 10^{18}$ g for a density of $\rho = 1$ g cm⁻³ (see others densities in Methods). Collisions occur only for sufficiently large critical inclination and wide initial separation, which overcomes LK quenching ($\alpha > \alpha_{\text{coll}}$, see Methods). The transition from secular to non-secular dominated regimes is given by

$$\alpha_t = 3^{1/3} \left[\frac{128}{135} \frac{(1 - e_{\text{out}}^2)}{\left(1 + \frac{2\sqrt{2}}{3} e_{\text{out}}\right)^2} \left(\frac{M_{\odot}}{m_{\text{in}}}\right)^{1/3} \frac{R_{\text{tot}}}{a_{\text{out}}} \right]^{1/4}, \quad (1)$$

or $\alpha_t \approx 0.174$ in our case. Fig. 1b demonstrates the separation in the non-secular regime prior to the collision. During the high-e phase, there are about ~ 10 cycles where the distance drops below 10^3 km. A collision occurs during the third LK cycle after about ~ 4600 yr. The mutual inclination flips its orientation during the high-e peak of the LK cycle (c). The eccentricity is essentially unbound and a collision eventually occurs (d).

In order to explore in detail the overall evolution and statistics of KBBs in the chaotic, non-secular regime, we defer to detailed N-body simulations, which provide us with the probability for collisions and post-collision characteristics. We use the publicly available code `REBOUND`¹⁸, with the `IAS15`¹⁹ integrator (see Methods for details and stopping conditions). We integrate four sets of initial conditions in the non-secular regime. Three sets include initial separations of $\alpha = 0.2, 0.3, 0.4$, and a fourth one with uniformly sampled separations. The orbital angles are sampled uniformly. The mutual inclination of observed binaries is cosine-uniform⁹, therefore we follow cosine-uniform sampling with a cut-off at $|\cos i| \leq 0.4$ (since lower inclinations cannot lead to a collision). For each case, we run 250 simulations (except for $\alpha = 0.2$, for which we run 200 simulations and $|\cos i| \leq 0.3$), each up to 5×10^4 yr.

Fig. 2 shows the cumulative distribution function (CDF) of various parameters of the colliding orbits. Both the closest approach $q = a(1 - e)/R_{\text{tot}}$ (**a**) and the final inclinations (**c**) at collision are consistent with a uniform distribution (in $\cos i$) between 40° and 140° , suggesting that the orbits are indeed chaotic and in the non-secular regime, as expected. Most orbits induce collisions after about a few thousand years (**b**). The mean collision time increases with increasing separation. The velocity at impact is comparable to the escape velocity with a very small dispersion, consistent with a gentle collision²⁰ (**d**).

We find the overall merger fractions of wide-binaries to be around 12% – 18% (see Extended Data Table 1), which is roughly consistent with the observed 10% – 25% contact-binaries for the cold classical belt²¹. Most mergers occur for initially high inclinations, as expected. A fraction of

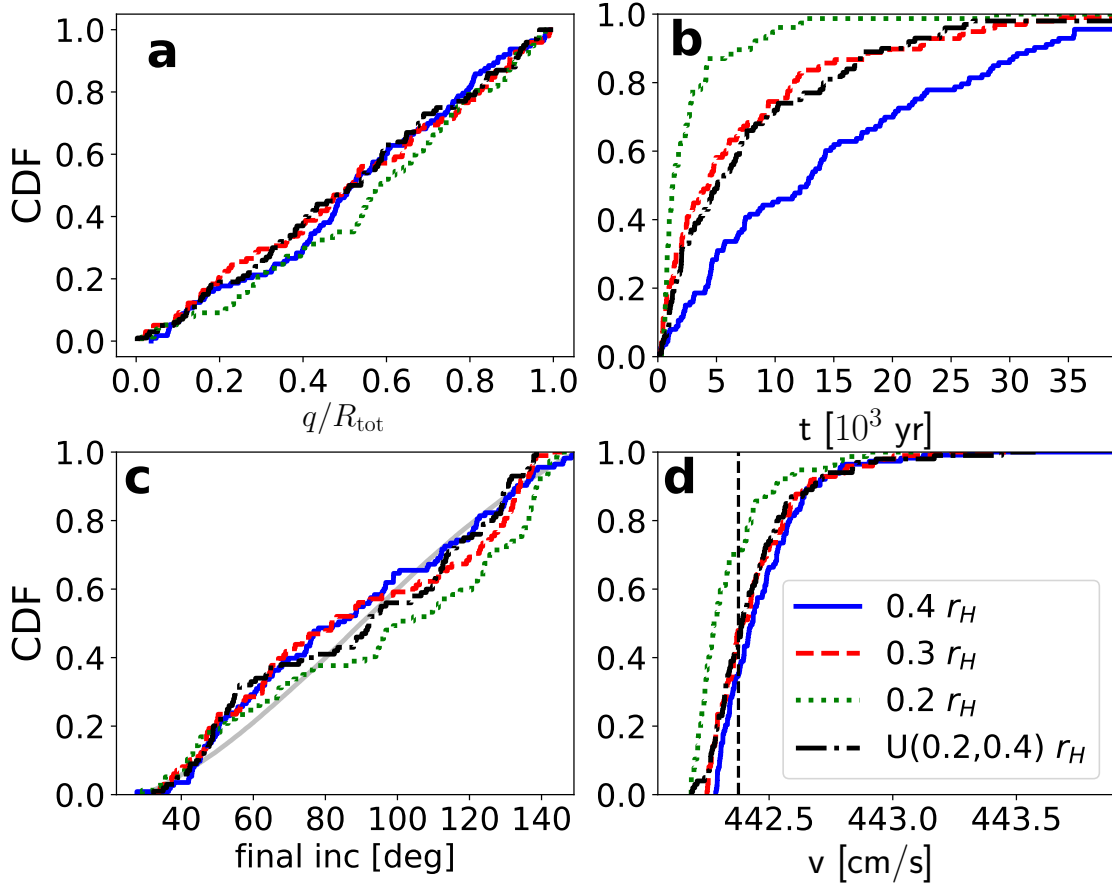


Figure 2: | **Cumulative distributions of the impact characteristics.** The CDFs are for $\alpha = 0.4$ (solid blue), 0.3 (dashed red), 0.2 (dotted green) and uniform in $(0.2, 0.4)$ (dash-dotted black). **(a)**, Pericentre q/R_{tot} . **(b)**, Time of collision. **(c)**, Final inclination at impact. The shaded grey line is a uniform cumulative distribution in $\cos i$ in the range of 30 – 150 deg. **(d)**, Velocity at impact. The vertical black dashed line is the escape velocity.

1% – 3% of the overall wide binaries produce highly oblique contact-binaries ($80^\circ - 100^\circ$), which are consistent with the observed high obliquity of MU₆₉ and provide clear predictions for future KBO observations with larger statistics. There is little dependence on the underlying distribution of α , and the merger rates are bounded between the minimal and maximal values of 12% for $\alpha = 0.2$ and 18% for $\alpha = 0.4$, respectively. Moreover, in a collisional environment²² the binary orbits can be perturbed such that originally low-inclination orbits become highly-inclined and be subjected to semi-secular evolution to form contact-binaries; the quoted formation rates are therefore only lower limits to the total fractions of contact-binaries formed through this process.

The non-merging systems will continue to evolve quasi-periodically. On longer timescales, three-body encounters are expected to shape the populations of KBBs^{3,23}. Exchange interactions can drive the binaries into equal masses²⁴, while the 'softness' of the binaries can make them become even softer and evaporate (Heggie's law²⁵). There is only a handful of KBBs beyond $a \gtrsim 0.05 r_H$ with either prograde or retrograde orbits, without highly inclined ones (see Fig 1 of ref.²⁶), while the widest known binary 2001 QW₃₂₂ at $a \approx 0.2 r_H$ is expected to disrupt within a billion years¹⁶.

In order to test the feasibility of MU₆₉'s semi-secular collision origin, we also need to account for the observed spin period of MU₆₉. Angular momentum conservation allows us to find the resulting spin period depending on the impact angle and the primordial spins of each component. The final impact parameter (which corresponds to an impact angle, see Methods) at collision is uniformly distributed, therefore our model can robustly produce a wide range of possible fi-

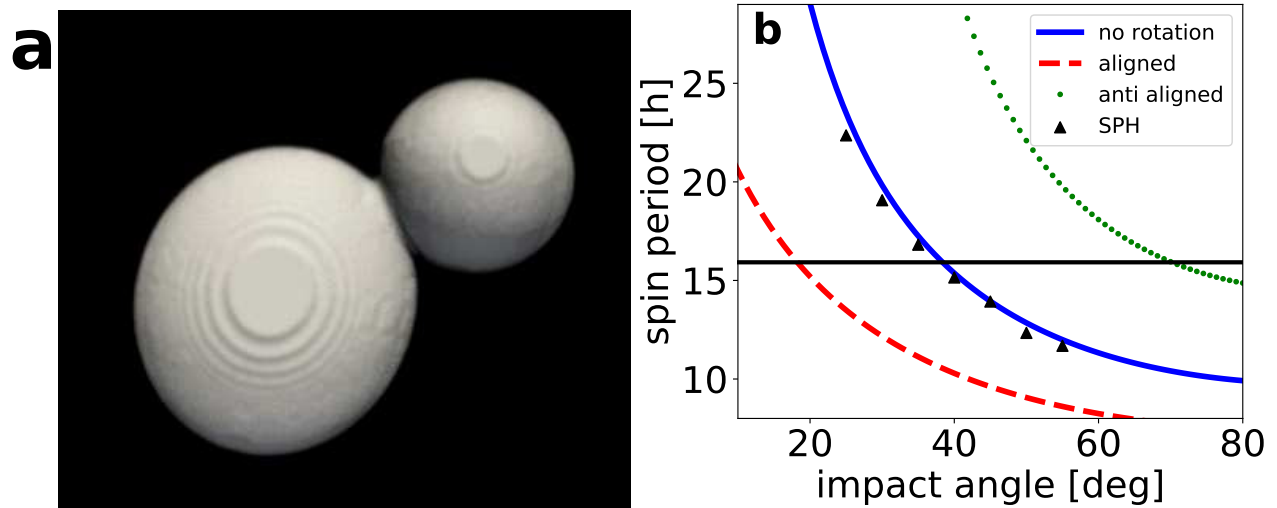


Figure 3: | **Shape and spin period of MU₆₉**. **(a)**, Final collision outcome at an impact angle of 40° with high material strength (see Methods). **(b)**, Spin period as a function of the impact angle for MU₆₉. The horizontal line is the observed period of 15.92 h. The solid blue line indicates initially non-rotating progenitors. The dashed red line indicates two initially aligned rotating progenitors with a period of 10 h, while the dotted green line indicates an anti-aligned configuration. The black crosses are the results obtained from SPH simulations (see Methods).

nal rotations periods, without any fine-tuned modelling of MU₆₉ and its composition/density, and alleviate the angular momentum problem, unlike other models¹.

Fig. 3a shows the outcome of a collision at a 40° impact angle with high material strength, which reproduces the shape of MU₆₉. Low or medium-strength materials result in a deformed shape and are thus ruled out. If MU₆₉'s density is halved compared to the fiducial 1g cm⁻³ value, as suggested by ref.¹, v_{esc} is lower, and in this case the medium-strength material also produces an undeformed shape. Random collisions, even at relative velocities as low as $10v_{\text{esc}}$ destroy or heavily deform the binary with high-strength materials, hence they are likewise ruled out (see Methods). Fig. 3b shows the expected spin period dependence on the impact angle. An impact angle of $\sim 40^\circ$ reproduces the observed spin period (see Methods) for initially non-spinning objects. Taking a typical initial spin period of ~ 10 h with random orientations extends the range of plausible impact angles to $\sim 20^\circ - 70^\circ$, for maximally aligned and anti-aligned configurations, respectively. Smoothed Particle Hydrodynamics (SPH) collision simulations agree with our simplified estimate and support our assumptions of undeformed, rigid bodies when modelled with high-strength material parameters, or else medium-high-strength parameters if the density/impact-velocity is slightly lower (see ref.²⁷ and Methods for details).

Together, our dynamical and post-collisional modelling yields a consistent, coherent picture for the origin of MU₆₉ from an ultra-wide KBO-binary. Such wide KBB progenitors could be a natural by-product of KBO and KBB evolution in the early Solar-System^{3,28,29}. Most likely the case of MU₆₉ is not unique, and secular/semi-secular evolution plays a major role in the evolution

of many KBBs and the production of low-velocity collisions between individual KBB components. In fact, modelling of the impact origin of the Pluto-Charon system also suggests a low-velocity impact is required to explain its properties³⁰. Moreover, given the high obliquity of the Pluto-Charon system, it is possible that it also had originated from an initially wide-binary and followed a secular/semi-secular evolution similar to MU₆₉. Similar evolutionary scenarios might also apply to the evolution of other contact binaries such as (139775) 2001 QG298² as well as moons and exo-moons, since all of them form hierarchical triple systems with their host star.

1. Stern, S. A. *et al.* Initial results from the new horizons exploration of 2014 mu69, a small kuiper belt object. *Science* **364**, eaaw6441.
2. Lacerda, P. A Change in the Light Curve of Kuiper Belt Contact Binary (139775) 2001 QG₂₉₈. *AJ* **142**, 90-98 (2011). 1107.3507.
3. Goldreich, P., Lithwick, Y. & Sari, R. Formation of Kuiper-belt binaries by dynamical friction and three-body encounters. *Nature* **420**, 643–646 (2002). astro-ph/0208490.
4. Richardson, D. C. & Walsh, K. J. Binary Minor Planets. *Annual Review of Earth and Planetary Sciences* **34**, 47–81 (2006).
5. Perets, H. B. & Naoz, S. Kozai Cycles, Tidal Friction, and the Dynamical Evolution of Binary Minor Planets. *ApJ Lett.* **699**, L17–L21 (2009). 0809.2095.
6. Antonini, F. & Perets, H. B. Secular Evolution of Compact Binaries near Massive Black Holes: Gravitational Wave Sources and Other Exotica. *ApJ* **757**, 27-40 (2012). 1203.2938.

7. Grishin, E., Perets, H. B. & Fragione, G. Quasi-secular evolution of mildly hierarchical triple systems: analytics and applications for GW sources and hot Jupiters. *MNRAS* **481**, 4907-4923 (2018).
8. Grishin, E., Perets, H. B., Zenati, Y. & Michaely, E. Generalized Hill-stability criteria for hierarchical three-body systems at arbitrary inclinations. *MNRAS* **466**, 276-285 (2017).
9. Naoz, S., Perets, H. B. & Ragozzine, D. The Observed Orbital Properties of Binary Minor Planets. *ApJ* **719**, 1775–1783 (2010). 1001.2558.
10. Lidov, M. L. The evolution of orbits of artificial satellites of planets under the action of gravitational perturbations of external bodies. *Planetary and Space Science* **9**, 719–759 (1962).
11. Kozai, Y. Secular perturbations of asteroids with high inclination and eccentricity. *AJ* **67**, 591-598 (1962).
12. Naoz, S. The Eccentric Kozai-Lidov Effect and Its Applications. *ARA&A* **54**, 441–489 (2016). 1601.07175.
13. Fabrycky, D. & Tremaine, S. Shrinking Binary and Planetary Orbits by Kozai Cycles with Tidal Friction. *ApJ* **669**, 1298–1315 (2007). 0705.4285.
14. Porter, S. B. & Grundy, W. M. KCTF evolution of trans-neptunian binaries: Connecting formation to observation. *Icarus* **220**, 947–957 (2012). 1206.5841.
15. Veillet, C. *et al.* The binary Kuiper-belt object 1998 WW31. *Nature* **416**, 711–713 (2002).
16. Petit, J. M. *et al.* The Extreme Kuiper Belt Binary 2001 QW₃₂₂. *Science* **322**, 432-434 (2008).

17. Luo, L., Katz, B. & Dong, S. Double-averaging can fail to characterize the long-term evolution of Lidov-Kozai Cycles and derivation of an analytical correction. *MNRAS* **458**, 3060–3074 (2016). 1601.04345.
18. Rein, H. & Liu, S.-F. REBOUND: an open-source multi-purpose N-body code for collisional dynamics. *A&A* **537**, A128 (2012). 1110.4876.
19. Rein, H. & Spiegel, D. S. IAS15: a fast, adaptive, high-order integrator for gravitational dynamics, accurate to machine precision over a billion orbits. *MNRAS* **446**, 1424–1437 (2015). 1409.4779.
20. McKinnon, W. B. *et al.* The solar nebula origin of (486958) arrokoth, a primordial contact binary in the kuiper belt. *Science* (2020). URL <https://science.sciencemag.org/content/early/2020/02/12/science.aay6620>.
<https://science.sciencemag.org/content/early/2020/02/12/science.aay6620.full.pdf>.
21. Thirouin, A. & Sheppard, S. S. Light Curves and Rotational Properties of the Pristine Cold Classical Kuiper Belt Objects. *AJ* **157**, 228-247 (2019). 1904.02207.
22. Parker, A. H. & Kavelaars, J. J. Collisional Evolution of Ultra-wide Trans-Neptunian Binaries. *ApJ* **744**, 139-152 (2012). 1111.2046.
23. Perets, H. B. Binary Planetesimals and Their Role in Planet Formation. *ApJ Lett.* **727**, L3, 5pp (2011). 1012.0567.

24. Funato, Y., Makino, J., Hut, P., Kokubo, E. & Kinoshita, D. The formation of Kuiper-belt binaries through exchange reactions. *Nature* **427**, 518–520 (2004). [astro-ph/0402328](#).
25. Heggie, D. C. Binary evolution in stellar dynamics. *MNRAS* **173**, 729–787 (1975).
26. Grundy, W. *et al.* Mutual orbit orientations of transneptunian binaries. *Icarus* **334**, 62-78 (2019).
27. Schäfer, C. *et al.* A smooth particle hydrodynamics code to model collisions between solid, self-gravitating objects. *Astronomy & Astrophysics* **590**, A19 (2016). [1604.03290](#).
28. Goldreich, P., Lithwick, Y. & Sari, R. Planet Formation by Coagulation: A Focus on Uranus and Neptune. *ARA&A* **42**, 549–601 (2004). [astro-ph/0405215](#).
29. Nesvorný, D., Li, R., Youdin, A. N., Simon, J. B. & Grundy, W. M. Trans-neptunian binaries as evidence for planetesimal formation by the streaming instability. *Nature Astronomy* **3**, 808-812 (2019).
30. Canup, R. M. A Giant Impact Origin of Pluto-Charon. *Science* **307**, 546–550 (2005).

Acknowledgements We gratefully acknowledge useful discussions with Daniel C. Fabrycky and Edwin Kite. HBP acknowledges support from the MINERVA center for "Life under extreme planetary conditions" and the Kingsley fellowship at Caltech. CMS and OW acknowledge support by the High Performance and Cloud Computing Group at the Zentrum für Datenverarbeitung of the University of Tübingen, the state of Baden-Württemberg through bwHPC and the German Research Foundation (DFG) through grant no INST 37/935-1 FUGG. CMS acknowledges support from the DFG through grant no 398488521.

Author information Correspondence and requests for materials should be addressed to EG (eugeneg@campus.technion.ac.il) and HBP (hperets@ph.technion.ac.il).

Methods

Lidov-Kozai secular evolution

Let us consider the evolution of a binary KBO due to LK secular evolution. Let the inner binary start with an initial separation of $a_0 = \alpha r_H$, eccentricity e_0 and mutual inclination i_0 . The Hill radius is $r_H = a_{\text{out}}(m_{\text{in}}/3M_{\odot})^{1/3}$. The most stable orbit is around $\alpha_H \approx 0.4$.⁸ The minimal eccentricity required for collision is

$$e_{\text{coll}} = 1 - \frac{R_{\text{tot}}}{\alpha r_H}. \quad (2)$$

Using the standard LK formula, the maximal eccentricity is

$$e_{\text{max}}^2 = 1 - \frac{5}{3}(1 - e_0^2) \cos^2 i_0. \quad (3)$$

In order for a collision occur, we require that $e_{\text{max}} \geq e_{\text{coll}}$, which yields the critical inclination

$$\cos i_0^c \approx \sqrt{\frac{6}{5(1 - e_0^2)} \frac{R_{\text{tot}}}{\alpha r_H}} = \frac{0.037}{\sqrt{1 - e_0^2}} \left(\frac{\alpha}{0.3}\right)^{-1/2}, \quad (4)$$

where $R_{\text{tot}}/r_H \ll 1$ was expanded to linear order. The probability for collision can be expressed in terms of integrating over the distribution function $f_{a,\theta}(a, \theta)$ and where $\theta \equiv \cos i$.

For uniform, independent distribution in $\cos i$, as inferred from KBO observations⁹, the probability is

$$P(e_0) = \int_{a_{\text{min}}}^{a_{\text{max}}} f_a(a) \theta_c(a) da, \quad (5)$$

where $\theta_c(a)$ is given by Eq. 4.

Inclination angle at impact: From the conservation of $j_z \equiv \sqrt{1 - e^2} \cos i$ the inclination at impact is

$$\cos i_{\text{coll}} = \frac{\sqrt{1 - e_0^2} \cos i_0}{\sqrt{1 - e_{\text{coll}}^2}} = \sqrt{1 - e_0^2} \cos i_0 \sqrt{\frac{\alpha r_H}{2R_{\text{tot}}}}. \quad (6)$$

In order to get an impact angle of i_{coll} , we invert Eq. 6:

$$i_0 = \arccos \left(\cos i_{\text{coll}} \sqrt{\frac{2R_{\text{tot}}}{\alpha r_H}} \right) \quad (7)$$

In order to get the observed obliquity $i_{\text{coll}} = 98^\circ$, the critical inclination is at least $|\cos i_0| \leq 0.00585$, ($89.33^\circ \leq i_0 \leq 90.66^\circ$) for $\alpha = 0.1$, which is unlikely. Moreover, for $\alpha \lesssim 0.1$, collisions are unlikely regardless of the initial inclination due to the effects of oblateness, as shown below.

Effects of oblateness: Small KBOs might not have spherical shapes, in which case their gravitational potential is not spherical. Such a configuration induces extra precession on the orbit which can significantly affect the secular evolution. The leading term is encapsulated in the J_2 coefficient of the gravitational potential³¹. Planets are mostly spherical, and their deviation is small; $J_2 \approx 10^{-3}$ for Earth and around $J_2 = 0.014$ for Jupiter, and is related to the flattening of the planets induced by their rotations. In the case of MU₆₉ components, the objects are highly non-spherical and J_2 could be large. Using the principal moments of inertia of an oblate spheroid, we have $J_2 = (1 - (c/a)^2)/5$, which is around $J_2 \approx 0.18$ for the primary and $J_2 \approx 0.1$ for the secondary.

The additional precession may quench the LK oscillations if it is too strong. In order to quantify the effects of the additional precession we can define a dimensionless quantity that measures the ratio between the LK and the oblateness induced precessions^{32,33}

$$\epsilon_{\text{rot}} = \frac{3}{2} J_2 \frac{m_{\text{in}}}{m_{\text{out}}} \frac{a_{\text{out}}^3 (1 - e_{\text{out}}^2)^{3/2} R_1^2}{(\alpha r_H)^5}, \quad (8)$$

Setting $\epsilon_{\text{rot}} = 3/2$ leads to the definition of the Laplace radius^{33,34} in terms of the Hill radius,

$r_L \equiv \alpha_L r_H$ where

$$\alpha_L = \left(J_2 \frac{m_{\text{in}}}{m_{\text{out}}} \right)^{1/5} \frac{(a_{\text{out}}^3 R_1^2)^{1/5}}{r_H} (1 - e_{\text{out}}^2)^{3/10} = 0.03 \left(\frac{J_2}{0.2} \right)^{1/5} \left(\frac{R_1}{11 \text{ km}} \right)^{2/5}, \quad (9)$$

leading to $\epsilon_{\text{rot}} = 1.5(\alpha/\alpha_L)^{-5}$.³² showed that the maximal eccentricity attained is given by the implicit expression for $\cos i_0 = 0$ (their Eq. 50):

$$\frac{\epsilon_{\text{rot}}}{3} \left(\frac{1}{(1 - e_{\text{max}}^2)^{3/2}} - 1 \right) = \frac{9}{8} e_{\text{max}}^2 \quad (10)$$

Expanding in $\epsilon_{\text{rot}} \ll 1$, $e_{\text{max}}^2 \approx 1$

$$e_{\text{max}} \approx 1 - \frac{2}{9} \epsilon_{\text{rot}}^{2/3}. \quad (11)$$

A collision can occur only if $e_{\text{coll}} < e_{\text{max}}$ or

$$\alpha_{\text{coll}} > \left(\frac{3}{2} \right)^{2/7} \alpha_L^{10/7} \left(\frac{2}{9} \frac{r_H}{R_{\text{tot}}} \right)^{3/7} \approx 0.12. \quad (12)$$

Note that a similar analysis can be made for tidal distortions or relativistic corrections³². In this case, they are much weaker than the rotational effects.

Non-secular Lidov-Kozai evolution

In the previous section we considered the evolution due to secular LK evolution. In the semi-secular (semi-LK) regime^{6,7}, short term fluctuations can significantly change the evolution. In the following we discuss the overall effects of such short-term perturbations. The strength of the perturbations is encapsulated in the single averaging parameter^{7,17}:

$$\epsilon_{\text{SA}} \equiv \left(\frac{a_1}{b_{\text{out}}} \right)^{3/2} \sqrt{\frac{m_{\text{out}}}{m_{\text{in}}}} = \frac{\alpha^{3/2}}{\sqrt{3}(1 - e_{\text{out}}^2)^{3/2}} \approx 0.1 \left(\frac{\alpha}{0.3} \right)^{3/2}. \quad (13)$$

One important quantity is the (averaged) z-angular momentum $\bar{j}_z = \sqrt{1 - e_0^2} \cos i_0$, assuming that i_0 and e_0 have their mean value.

The eccentricity of the orbit becomes unbound once the fluctuation in j_z , Δj_z is larger than its initial value, namely $\Delta j_z > \bar{j}_z$. The fluctuation is estimated analytically in^{7,17}, and can be used to show that the eccentricity is unbound if

$$\cos i_0 \sqrt{1 - e_0^2} \lesssim \frac{9}{8} \tilde{\epsilon}_{\text{SA}} \approx 0.118 \left(\frac{\alpha}{0.3} \right)^{3/2}, \quad (14)$$

where $\tilde{\epsilon}_{\text{SA}} = \epsilon_{\text{SA}} (1 + 2\sqrt{2}e_{\text{out}}/3) \approx 1.039\epsilon_{\text{SA}}$ is defined for convenience.

The width of the non-secular semi-LK regime increases with α , while the width of the secular LK regime decreases with increasing α . Comparing Eq. (4) and Eq. (14) yields the transitional separation α_t found in Eq. 1.

Spin period

There is little evidence for structural changes of the object since its formation, and the spin period is believed to be primordial¹. In our model, the collision is gentle and occurs at relatively

low velocities ($v_{\text{esc}} = 442.4 \text{ cm s}^{-1}$ for our nominal density and $v_{\text{esc}} = 3.12.8 \text{ cm s}^{-1}$ for the lower density of 0.5 g cm^{-3} assumed in ref.¹), such that almost any impact parameter (or impact angle) is allowed. Therefore, in order to obtain the observed spin period, we can use the standard arguments of angular momentum conservation and derive the impact parameter (or impact angle) that yields the desired spin rate.

Consider triaxial ellipsoidal bodies with masses m_i and axes $a_i \geq b_i \geq c_i$, with $i = 1, 2$. We assume that the major axes a_i are parallel, similar to the observed object, and that the collision occurs also in parallel with the major axes. The largest moment of inertia is $I_3^{(i)} = m_i(a_i^2 + b_i^2)/5$.

After the collision the distance between the centre of masses of the joint body and each centre of the ellipsoid is r_i . Then the principal moment of inertia of the joint body is

$$I_3^{\text{tot}} = I_3^{(1)} + I_3^{(2)} + m_1 r_1^2 + m_2 r_2^2 = \sum_{i=1}^2 \frac{m_i}{5} (a_i^2 + b_i^2 + 5r_i^2).$$

Now, the ellipsoids collide with relative velocity v_{esc} and impact parameter b . The orbital angular momentum is $L_z = \mu b v_{\text{esc}}$, where $\mu = m_1 m_2 / (m_1 + m_2)$ is the reduced mass. If the two bodies are non-rotating, then the joint angular frequency is

$$\Omega = \frac{L_z}{I_3^{\text{tot}}} = \frac{5\mu b v_0}{m_1 (a_1^2 + b_1^2 + 5r_1^2) + m_2 (a_2^2 + b_2^2 + 5r_2^2)}. \quad (15)$$

If the individual bodies are rotating around the z axis with frequencies Ω_i , the additional angular momentum of each body is $I_3^{(i)} \Omega_i$ for $i = 1, 2$, thus Eq. (15) becomes

$$\Omega = \frac{5\mu b v_0 + m_1 (a_1^2 + b_1^2) \Omega_1 + m_2 (a_2^2 + b_2^2) \Omega_2}{m_1 (a_1^2 + b_1^2 + 5r_1^2) + m_2 (a_2^2 + b_2^2 + 5r_2^2)}. \quad (16)$$

For an impact angle θ , the distance of the point of contact to the centre of each ellipsoid is $\xi_i = \sqrt{a_i^2 \cos^2 \theta + b_i^2 \sin^2 \theta}$. The impact parameter is related to the impact angle by $\sin \theta = b/(\xi_1 + \xi_2) = b/d$. The distances from the centre of mass are $r_1 = m_2 d/(m_1 + m_2)$ and $r_2 = m_1 d/(m_1 + m_2)$, and the spin rate is

$$\Omega = \frac{5\mu d v_{\text{esc}} \sin \theta + m_1(a_1^2 + b_1^2)\Omega_1 + m_2(a_2^2 + b_2^2)\Omega_2}{5\mu d^2 + m_1(a_1^2 + b_1^2) + m_2(a_2^2 + b_2^2)}. \quad (17)$$

Fig. 3 shows the spin period dependence on the impact angle for the typical parameters of MU₆₉. The spin period is $P = 2\pi/\Omega$, where Ω is given by Eq. (17), with no internal rotation $\Omega_1 = \Omega_2 = 0$. We see that an impact angle of $\sim 40^\circ$ gives the observed spin period. We have performed hydrodynamical simulations based on the code of ref.²⁷ that qualitatively agree with our assumptions and reproduce similar results. Typical classical KBO objects could have primordial spin periods³⁵ with comparable contributions to the angular momentum budget. Recently, ref.²¹ found that the average cold classical KBO spin periods are 9.48 ± 1.53 h. Generally, there is no reason for the spin vectors of each body to be correlated, so on average the contribution is zero. In extreme cases, the spin vector of both objects could be aligned or anti-aligned with the orbital angular momentum. In these cases, a wide range of impact angles and spin configurations are possible, resulting in the observed spin period after the collision. For a typical period of 10 h, the impact angle is $\sim 20^\circ$ in the aligned case, and $\sim 70^\circ$ in the anti-aligned case.

N-body stopping conditions and tests

We impose a stopping condition that the distance between the two bodies is less than their mutual radius. During the non-secular highly eccentric passage, the change in the pericentre q is much faster than the *inner* orbital period (it is actually the definition of the non-secular regime), hence the orbital elements are not reliable at this stage. Once the simulation stops it records the orbital elements *at impact* which we use for our statistics, but are not involved in the stopping condition. From the output we know the closest approach at impact. We have tested the stopping condition by varying it to be slightly smaller or larger than the q we found in the first run. Indeed when the stopping condition was below q the objects did not collide and continued running. We thereby concluded that the collision is physical and reliable.

Extended Data Table 1 shows the merger fractions from the simulations. The merger fraction f_i is the total number of mergers divided by the initial number of runs, multiplied by the relative fractions of the inclination distribution, assuming that no mergers occur outside the sampled inclination distribution. The fraction f_{80-100} is calculated in the same way, only that the mergers considered are where the mutual inclination during the merger is within the designated boundaries of $80^\circ - 100^\circ$. For example, for $\alpha = 0.2$, the merger fractions is $78/200 = 0.39$. Multiplied by the range of the inclination distribution it is $f_i = 0.39 \times 0.3 \approx 0.12$. For $\alpha = 0.3$, the merger fractions is $99/250 = 0.396$. Multiplied by the range of the inclination distribution it is $f_i = 0.396 \times 0.4 = 0.158$.

Impact modelling

We perform hydrodynamical collision simulations using our SPH code²⁷, which treats self-gravity, gas, fluid, elastic, and plastic solid bodies with material strength, including a porosity and fracture model that can be applied for small-body collisions^{36,37}. In order to treat numerical rotational instabilities, a tensorial correction scheme³⁸ is implemented. The *miluphCUDA* code is implemented with CUDA, and runs on graphics processing units (GPU), with a substantial $\sim 10^1 - 10^2$ improvement for single GPU compared to a single CPU. The code has already been successfully applied to several studies involving impact processes^{36,37,39-47}.

For the porosity treatment, we implement the $P-\alpha$ model^{48,49}, where the pores are much smaller than the spatial resolution and cannot be modelled explicitly. Here, the total change in the volume depends on both the compaction/collapse of the pore space, and the compression of the solid material which constitutes the matrix. The dependence is expressed in terms of the porous material pressure P and density ϱ as $P/\varrho = P_s/\varrho_s$, where P_s and ϱ_s are the pressure and density of the *solid* matrix material, respectively. The distention parameter $\bar{\alpha} = \varrho_s/\varrho$ is the ratio between the solid matrix material and the porous material densities, and relates to the porosity ψ via $\psi = 1 - 1/\bar{\alpha}$. For the solid matrix material we use the Tillotson equation of state (EOS) parameters⁵⁰ with a reduced bulk modulus of $A = 2.67 \times 10^8$ Pa (leading term in the EOS) in order to consistently take into account the smaller elastic wave speeds in porous compared to solid materials, and in compatibility with ref.⁵¹. Our matrix density is chosen to be 2 g cm^{-3} , about the same as that of ref.⁵², which leads to a 50% porosity for our fiducial bulk density for MU₆₉, 1 g cm^{-3} . The matrix density and the initial porosity are

both in rough agreement with what might be expected from an object of this origin and size range. The former in particular, constraints the rock/ice mass ratio to be about 3-4 (depending on the exact choice of silicate grain density), which could be compatible with this kind of object⁵³⁻⁵⁶. We note however that given the uncertainties involved, we only seek to obtain a rough estimate of the density which will permit us to test our working hypothesis. We then also test some simulations with 75% porosity and half the previous bulk density, in order to establish qualitative differences among these two setups.

For collisions between small, porous bodies, compressibility is limited by the crush curve for $\bar{\alpha}$ for typical pressures, rather than the Tillotson EOS parameters. We thereby choose three sets of crush curve parameters, similarly to ref.⁵², using a simple quadratic crush curve⁵⁷:

$$\bar{\alpha} = 1 + (\bar{\alpha}_0 - 1) \frac{(P_s - P)^2}{(P_s - P_e)^2}, \quad (18)$$

where $\bar{\alpha}_0 = 2$, P_e is the transition pressure between the elastic and plastic regimes and P_s is the pressure of full compaction. Both P_e and P_s are listed in the Extended Data Table 2. Since ref.⁵² treats comet 67P/Churyumov-Gerasimenko, which belongs to a class of much smaller and active objects, we assume it is likely to be a lot more fluffier and porous. Hence our low-strength crush curve values correspond to the high-strength values from⁵², and taking the same modeling approach, we then increment the parameters in each subsequent model by one order of magnitude.

Fracture and brittle failure are treated using the Grady and Kipp fragmentation prescription⁵⁸⁻⁶⁰, which is based on randomly distributed flaws in the material following a Weibull distribution with material-dependent parameters. The lowest activation threshold

Extended Data Table 1| Merger rate of the binaries in the non-secular regime. Top to bottom: N_m - total number of mergers. N_{80-100} - number of merger with inclination $80^\circ < i < 100^\circ$. f_i - total merger fraction normalized to the inclination sampling rate. f_{80-100} - the same merger fraction, only with merger at inclination $80^\circ < i < 100^\circ$.

	0.2	0.3	0.4	U
N_m	78	99	114	101
N_{80-100}	9	12	18	15
f_i	0.12	0.158	0.18	0.16
f_{80-100}	0.014	0.015	0.029	0.02

Extended Data Table 2| Crush curve, plasticity and fragmentation parameters.

Type	P_e (Pa)	P_s (Pa)	Y_0 (Pa)	Y_T (Pa)
Low-strength	10^4	10^6	10^4	10^3
Medium-strength	10^5	10^7	10^5	10^4
High-strength	10^6	10^8	10^6	10^5

strain derived from the Weibull distribution, is given by $\epsilon = kV^{-1/m}$, where V is the volume of the brittle material and k and m are the material dependent Weibull parameters. We adopt $m = 9.5$ for pressure-dependent failure⁶¹. The volume is calculated given the MU_{69} binary dimensions. From the material strength parameters K and G , Young's modulus E may be calculated as $E = (9KG)/(3K + G)$. Here $K = 2.67 \times 10^8$ Pa, as is the leading term in the Tillotson EOS, and $G = 1.6 \times 10^8$ Pa. Finally, for undamaged material $\epsilon = Y_T/E$, where Y_T is the tensile strength in Table 30⁵². Therefore, k may be extracted and equals to $k = 10^{47}, 2 \times 10^{39}, 2 \times 10^{28} \text{ m}^{-3}$ for the low, medium and high-strength material setups, respectively. Damage accumulates when the local tensile strain reaches the activation threshold of a flaw.

For the plasticity model we use a pressure-dependent yield strength⁶² with the implementation of ref.⁶¹. The yield stress Y_i is different for damaged/intact material. For intact material the yield stress is $Y_i = Y_0 + \mu_i P / (1 + \mu_i P / (Y_M - Y_0))$, where Y_0 is the cohesion (see Table 30), μ_i is the coefficient of friction and Y_M is the shear strength at $P = \infty$. We adopt $\mu_i = 1.5$ ⁶¹ and a typical $Y_M = 1.5 \times 10^9$ Pa⁶⁰, which is appropriate for an object composed of ice, rock and organics. For $P = 0$, we recover the pressure-independent form $Y_i = Y_0$. For damaged material the yield stress is $Y_d = \mu_d P$, where μ_d is the coefficient of friction of the damaged material. Here we take $\mu_d = 0.6$ following ref.⁶¹, thus fully damaged particles still undergo some shear stress.

Extended Data Figure 1 shows additional results of our simulated impacts. We obtain the MU_{69} rotation period, using the nominal density of 1 g cm^{-3} , only when using the high-

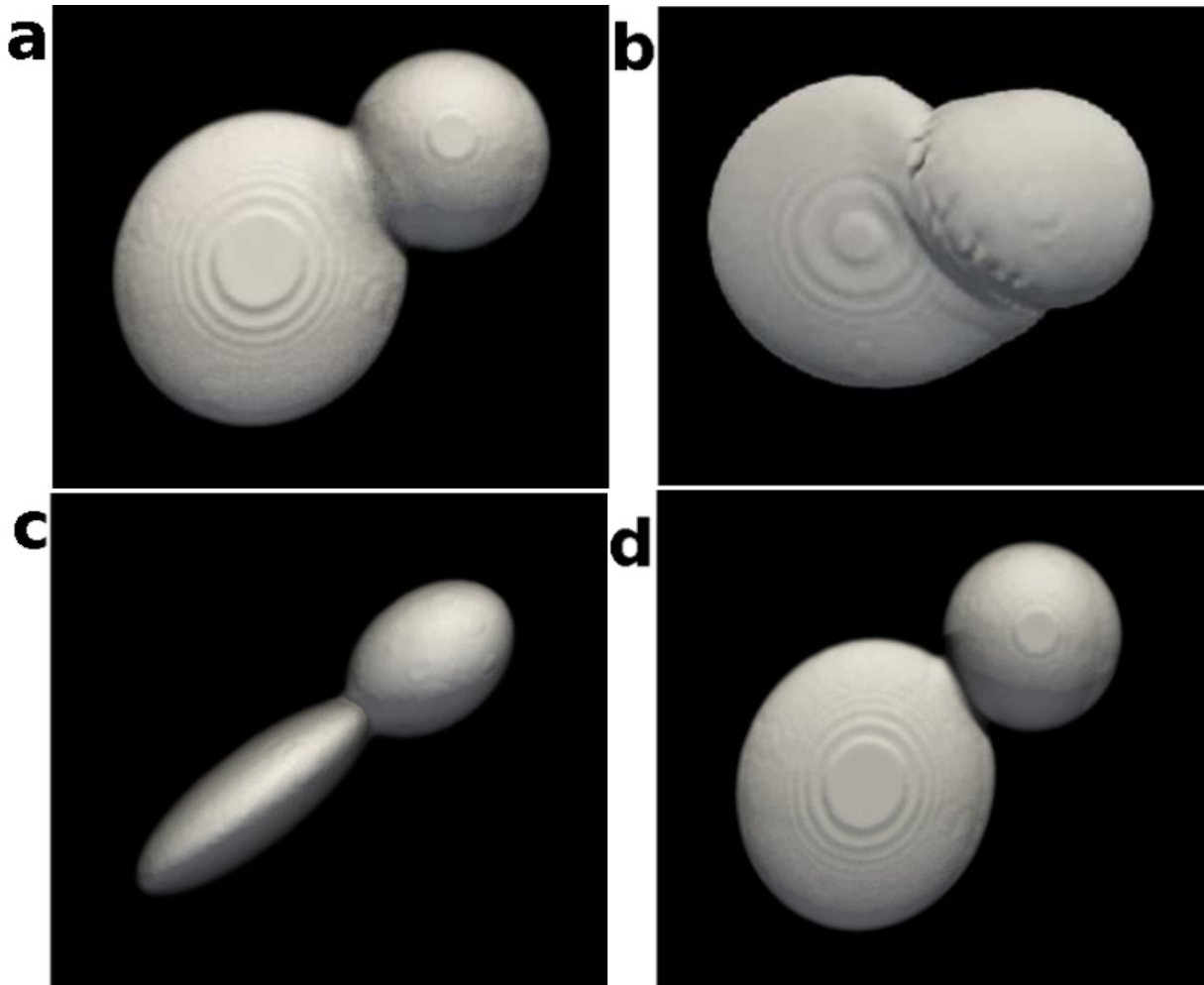


Figure 4: **Extended Data Fig. 1** | **Additional results of the collision models.** (a), 40° impact angle, medium-strength material. (b), 40° impact angle, low-strength material. (c)-(d), Low 0.5 g cm⁻³ density model with impact angle of 55° and medium-strength material. (c), Edge view. (d), Face view.

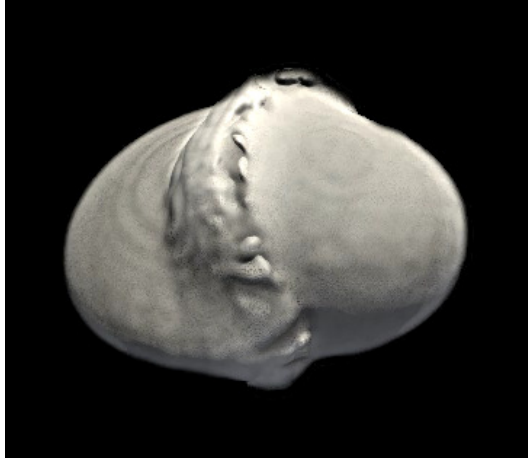


Figure 5: **Extended Data Fig. 2| Additional results of the collision models.** 5° impact angle, high-strength material, large $v = 10v_{\text{esc}}$ escape velocity.

strength material parameters. Medium **(a)** or low **(b)** strength materials deform MU₆₉ and do not produce the observed shape of a gently merged contact binary. If the nominal density is halved (0.5 g cm^{-3}), the v_{esc} impact velocity is lower, which produces less deformation in our simulations. Even medium-strength material parameters generate a gently merged contact binary for virtually all impact angles **(c)-(d)**. Here, we used the 55° impact angle, for which the observed spin period of MU₆₉ is approximately obtained. In Extended Data Fig. 2 the shape is significantly deformed after the collision if the impact velocity is large $v = 10 v_{\text{esc}}$, using high-strength material parameters. The same velocity with weaker material parameters further leads to a complete disruption.

Our simulations were performed for a grid of impact angles, assuming pre-alignment of the two lobes. Simulating higher impact angles and low and medium strength materials causes the two lobes to interact in other ways: In some cases they hit and create contact craters,

and then roll on top of each other. In other cases they stroke through each other and bounce instead of roll, and then return to re-collide following a (now) shorter orbital period. These formation channels may also generate compatible shapes but (so far) not yet the exact MU_{69} rotation period. In fact, a full investigation of the collision phase space must also include pre-self-rotation of each lobe, in addition to inclined hits. This entails a huge collision phase space exceeding the scope of this work, and necessitates a dedicated hydrodynamical study. Preliminary results (in preparation) indicate that such an approach may yield more channels which might generate the unique orientation of MU_{69} , besides the successful cases (of a pre-aligned binary components) shown here.

Our standard resolution is 5×10^5 SPH particles. We have additionally preformed simulations with 10^5 and 2.5×10^5 particles. Test Simulations were performed on the 'TAMNUN' GPU cluster, at the Technion Institute in Israel, and production runs on the bwForCluster BinAC, at Tübingen University.

31. Murray, C. D. & Dermott, S. F. *Solar system dynamics* (Cambridge University Press, 1999).
32. Liu, B., Muñoz, D. J. & Lai, D. Suppression of extreme orbital evolution in triple systems with short-range forces. *MNRAS* **447**, 747–764 (2015). 1409.6717.
33. Grishin, E., Lai, D. & Perets, H. B. Chaotic quadruple secular evolution and the production of misaligned exomoons and Warm Jupiters in stellar multiples. *MNRAS* **474**, 3547–3556 (2018). 1710.05920.

34. Tremaine, S., Touma, J. & Namouni, F. Satellite Dynamics on the Laplace Surface. *AJ* **137**, 3706–3717 (2009). 0809.0237.
35. Thirouin, A., Noll, K. S., Ortiz, J. L. & Morales, N. Rotational properties of the binary and non-binary populations in the trans-Neptunian belt. *A&A* **569**, A3 (2014). 1407.1214.
36. Wandel, O. J., Schäfer, C. M. & Maindl, T. I. Collisional fragmentation of porous objects in planetary systems. *Proceedings of the First Greek-Austrian Workshop on Extrasolar Planetary Systems* 225–242 (2017).
37. Haghhighipour, N., Maindl, T. I., Schäfer, C. M. & Wandel, O. J. Triggering the activation of main-belt comets: The effect of porosity. *The Astrophysical Journal* **855**, 60 (2018). 1801.08247.
38. Speith, R. Improvements of the numerical method smoothed particle hydrodynamics (2006). Habilitation Thesis.
39. Dvorak, R., Maindl, T. I., Burger, C., Schäfer, C. & Speith, R. Planetary systems and the formation of habitable planets. *Nonlinear Phenomena in Complex Systems* **18**, 310–325 (2015). 1502.02937.
40. Maindl, T. I. *et al.* Impact induced surface heating by planetesimals on early mars. *Astronomy & Astrophysics* **574**, A22 (2015). 1405.5913.
41. Haghhighipour, N., Maindl, T. I., Schäfer, C., Speith, R. & Dvorak, R. Triggering sublimation-driven activity of main belt comets. *The Astrophysical Journal* **830**, 22 (2016). 1606.06226.

42. Schäfer, C. M. *et al.* Numerical simulations of regolith sampling processes. *Planetary and Space Science* **141**, 35–44 (2017). 1705.00893.
43. Burger, C., Maindl, T. I. & Schäfer, C. M. Transfer, loss and physical processing of water in hit-and-run collisions of planetary embryos. *Celestial Mechanics and Dynamical Astronomy* **130** (2018). 1710.03669.
44. Malamud, U., Perets, H. B., Schäfer, C. & Burger, C. Moonfalls: collisions between the earth and its past moons. *Monthly Notices of the Royal Astronomical Society* **479**, 1711–1721 (2018). 1805.00019.
45. Malamud, U., Perets, H. B., Schäfer, C. & Burger, C. Collisional formation of massive exomoons of superterrestrial exoplanets. *MNRAS* **492**, 5089–5101 (2020).
46. Malamud, U. & Perets, H. B. Tidal disruption of planetary bodies by white dwarfs I: A hybrid SPH-analytical approach. *MNRAS* **128** (2020). 1911.12068.
47. Malamud, U. & Perets, H. B. Tidal disruption of planetary bodies by white dwarfs II: Debris disc structure and ejected interstellar asteroids. *MNRAS* **129** (2020). 1911.12184.
48. Herrmann, W. Constitutive equation for the dynamic compaction of ductile porous materials. *Journal of Applied Physics* **40**, 2490–2499 (1969).
49. Carrol, M. & Holt, A. C. Suggested modification of the α model for porous material. *Journal of Applied Physics* **43**, 759–761 (1972).

50. Jutzi, M., Michel, P., Hiraoka, K., Nakamura, A. M. & Benz, W. Numerical simulations of impacts involving porous bodies. ii. comparison with laboratory experiments. *Icarus* **201**, 802–813 (2009).
51. Leleu, A., Jutzi, M. & Rubin, M. The peculiar shapes of Saturn’s small inner moons as evidence of mergers of similar-sized moonlets. *Nature Astronomy* **2**, 555–561 (2018). 1805.08682.
52. Jutzi, M., Benz, W., Toliou, A., Morbidelli, A. & Brasser, R. How primordial is the structure of comet 67p?. combined collisional and dynamical models suggest a late formation. *Astronomy & Astrophysics* **597**, A61 (2017). 1611.02604.
53. Rotundi, A. *et al.* Dust measurements in the coma of comet 67p/churyumov-gerasimenko inbound to the sun. *Science* **347**, aaa3905 (2015).
54. Malamud, U. & Prialnik, D. Modeling kuiper belt objects charon, orcus and salacia by means of a new equation of state for porous icy bodies. *Icarus* **246**, 21–36 (2015).
55. Lorek, S., Gundlach, B., Lacerda, P. & Blum, J. Comet formation in collapsing pebble clouds. what cometary bulk density implies for the cloud mass and dust-to-ice ratio. *Astronomy & Astrophysics* **587**, A128 (2016). 1601.05726.
56. Fulle, M. *et al.* The dust-to-ices ratio in comets and kuiper belt objects. *Monthly Notices of the Royal Astronomical Society* **469**, S45–S49 (2017).

57. Jutzi, M., Benz, W. & Michel, P. Numerical simulations of impacts involving porous bodies. i. implementing sub-resolution porosity in a 3d sph hydrocode. *Icarus* **198**, 242–255 (2008).
0807.1264.
58. E. Grady, D. & E. Kipp, M. *Dynamic Fracture and Fragmentation*, 265–322 (Springer, New York, NY, 1993).
59. Benz, W. & Asphaug, E. Impact simulations with fracture. i - method and tests. *Icarus* **107**, 98 (1994).
60. Benz, W. & Asphaug, E. Catastrophic disruptions revisited. *Icarus* **142**, 5–20 (1999).
astro-ph/9907117.
61. Jutzi, M. SPH calculations of asteroid disruptions: The role of pressure dependent failure models. *Planetary and Space Science* **107**, 3–9 (2015). 1502.01860.
62. Collins, G. S., Melosh, H. J. & Ivanov, B. A. Modeling damage and deformation in impact simulations. *Meteoritics and Planetary Science* **39**, 217–231 (2004).